CrossMark

Microstructure and Mechanical Properties of Laser Solid Formed Ti-6Al-4V Alloy Under Dynamic Shear Loading

Ping Zhou, Wei-Guo Guo, Yu Su, Jianjun Wang, Xin Lin, and Weidong Huang

To investigate the mechanical properties of the Ti-6Al-4V alloy fabricated by laser solid forming technology, both static and dynamic shear tests were conducted on hat-shaped specimens by a servohydraulic testing machine and an enhanced split Hopkinson pressure bar system, over a temperature range of 173-573 K. The microstructure of both the original and deformed specimens was characterized by optical microscopy and scanning electron microscopy. The results show that: (1) the anisotropy of shear properties is not significant regardless of the visible stratification and the prior-β grains that grow epitaxially along the depositing direction; (2) the ultimate shear strength of this material is lower than that of those Ti-6Al-4V alloys fabricated by forging and extrusion; (3) the adiabatic shear bands of approximately 25.6-36.4 μm in width can develop at all selected temperatures during the dynamic shear deformation; and (4) the observed microstructure and measured microhardness indicate that the grains become refined in adiabatic shear band. Estimation of the temperature rise shows that the temperature in shear band exceeds the recrystallization temperature. The process of rotational dynamic recrystallization is considered to be the cause of the grain refinement in shear band.

1. Introduction

Ti-6Al-4V alloy has become the most widely used and relatively economical titanium alloy. There are many applications for this two-phase $\alpha + \beta$-type alloy, principally in the aerospace industry. Examples of applications are for fasteners, engine components and load-carrying components. However, to manufacture the products with complex and/or irregular geometrical shapes, the traditional material processing technologies usually result in high buy-to-fly ratio and long lead time for production. Laser solid forming (LSF) technology, which is a solid freeform manufacture method, can be employed in near-net-shape fabricating of metallic components. This technology has great potential for the fabrication of aerospace components.

Many studies were conducted on the LSF technology of titanium alloys, including Ti-6Al-4V alloy. The processing parameters for LSF were analyzed by the Air Force Research Laboratory in 1997, and the properties of the Ti-6Al-4V alloy fabricated with LSF (designated as Ti-6Al-4V alloy (LSF) hereafter) were evaluated (Ref 1, 2). Kobryn et al. (Ref 3) discussed the influence of processing parameters on the

microstructure, the porosity and the build height of Ti-6Al-4V alloy (LSF). Bontha et al. (Ref 4) observed the effects of processing variables on the grain morphologies of Ti-6Al-4V alloy (LSF). Zhang et al. (Ref 5) showed that with the decreasing cooling rates and the increasing solution temperatures, the primary α-laths in Ti-6Al-4V alloy (LSF) exhibit an increase in width and a decrease in the volume fraction and aspect ratio. Such phenomena lead to lower hardness, lower tensile strength and higher ductility of this material. Li et al. (Ref 6) investigated the plastic flow behavior of the Ti-6Al-4V alloy fabricated by 3D laser deposition technology under tensile and compressive loading. They considered the initial defects as an important source for the crack initiation and propagation.

As it has been shown, most of the previous studies are focused on the formation process, the microstructural characteristics, the influence of the processing parameters, and the tensile and compressive properties of Ti-6Al-4V alloy (LSF). Shear test is also a very useful method that can be used to study the mechanical behaviors of metals because they basically deform plastically by shear (Ref 7). The shear test not only provides a fundamental loading mode, but also has advantages over the uniaxial tension and compression tests, which are used more frequently. The advantages of shear test mainly include: (1) larger strains and higher strain rates generally can be reached in shear test, by which better material modeling is achieved, (2) shear test is useful for some materials to study the mechanisms leading to shear localization and (3) an unambiguous relation exists between true and engineering values of the stress since there is no cross-sectional reduction in the specimen subjected to shear (Ref 8). Moreover, in many technical applications metals are often loaded either statically or dynamically in shear (machining, deburring, blanking, impact, etc.). In the case of shearing, the deformation may become unstable, which can result in the onset of adiabatic shear bands (ASBs) followed by possible fracturing (Ref 7). Also, the initial microstructure of Ti-6Al-4V alloy (LSF) is unique compared with that of conventional processed Ti-6Al-4V alloys. The

Ping Zhou, Wei-Guo Guo, and **Jianjun Wang**, School of Aeronautics, Northwestern Polytechnical University, Xi'an 710072, China; **Yu Su**, Department of Mechanics, School of Aerospace Engineering, Beijing Institute of Technology, Beijing 100081, China; and **Xin Lin** and **Weidong Huang**, State Key Laboratory of Solidification Processing, Northwestern Polytechnical University, Xi'an 710072, China. Contact e-mail: weiguo@nwpu.edu.cn.

unique characteristics of this alloy is caused by high-temperature melting followed by rapid cooling of Ti-6Al-4V powders, so that some manufacturing defects may exist in the initial microstructure. Therefore, investigations on the dynamic shear behaviors of Ti-6Al-4V alloy (LSF), together with the related study of adiabatic shear band, are indispensable.

The aim of this work is to evaluate the mechanical responses of Ti-6Al-4V alloy (LSF) under static or dynamic shear loading with the selected initial temperatures of 173, 293 and 573 K. Static and dynamic compression tests were also carried out for reference and comparison purpose. The microstructure of both the original and deformed specimens was characterized by optical microscopy (OM) and scanning electron microscopy (SEM). Finally, the grain refinement in adiabatic shear band was discussed. The results from this work will not only provide an understanding of the mechanical response and microstructural characteristics of Ti-6Al-4V alloy (LSF) under shear loading, but also provide insights for improving the shear resistance of such materials.

2. Material and Experimental Procedures

2.1 Material

The investigated material was selected to be Ti-6Al-4V alloy (LSF). A LSF system consisting of a continuous wave CO_2 laser, a powder feeder with a coaxial nozzle, and a four-axis numerical control worktable was used in the fabrication process. A schematic illustration of the LSF setup is presented in Fig. 1. The substrate was pure titanium plate. Gas-atomized Ti-6Al-4V alloy powders of 100-150 μm in diameter were used in the process. The chemical composition of the Ti-6Al-4V powders (in wt pct) was: 6.02 Al, 4.00 V, 0.098 Fe, 0.033 Si, 0.025 C, 0.04 N, 0.008 H, 0.16 O and the balance of Ti. The fabrication process was conducted inside a controlled atmosphere box that was filled with argon gas. The oxygen content was lower than 150 ppm in this box to keep the melting pool from oxidizing. The processing parameters of the LSF route are
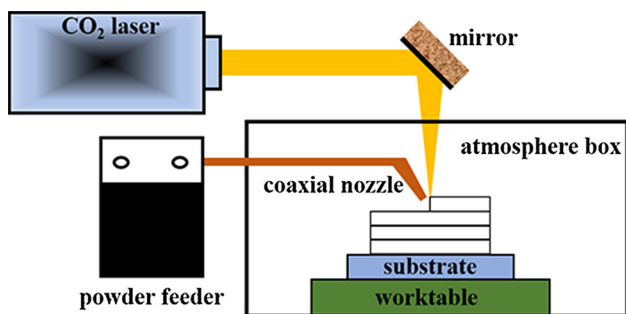

Fig. 1 Schematic of the LSF setup

summarized in Table 1. The Ti-6Al-4V alloy (LSF) used in this work was in the so-called as-deposited condition.

The LSF technology was used to produce a cubical block of Ti-6Al-4V alloy and the dimensions were approximately 80 mm × 53 mm × 60 mm. Specimens were sliced from the block along the Y-direction and Z-direction, respectively. The Y-direction represents the laser scanning direction, while the Z-direction represents the depositing direction. Then the specimens were stress relief annealed at 500 °C for 4 h and were cooled in furnace (Ref 9).

As shown in Fig. 2(a), the stratification and layer bands exist along the Z-direction. The thickness of layer bands is 1-3 mm approximately. This stratification is caused by the repeating melting-solidification process. It can be seen that an epitaxial columnar prior-β grain grows across a few layer bands. The growth direction of β grain is along the Z-direction and is inclined to the Y-direction slightly. The spacing of β grains is approximately 300-500 μm, and the length is a few millimeters. The perimeters of the prior-β grains are decorated with α-phase grain boundaries. The crystallographic microstructure in the β grains is composed of a string of needle-like α phase, a lot of Widmanstätten α-laths and a few β phases between α-laths (Fig. 2b and c). The microstructure of needle-like α phase and Widmanstätten α-laths is both thin and in needle shape. This microstructure has high strength and is harmful to the plasticity. Figure 2(b) shows that there is a lot of α-lamellae phase that precipitates along the β grain boundary. Such phenomenon causes the dislocation glide easily and leads to the lower yield strength. Figure 2(c) shows that the Widmanstätten α-laths are coarsened along the β grain boundary. These coarse Widmanstätten α-laths can decrease the inhibition of the dislocation glide and reduce the strength of this alloy. Meanwhile, they improve the plasticity and the synergy deformation ability.

The microhardness measurement results indicate that no distinct difference exists in microhardness between the layer bands and of the layer interiors. The microhardness of the layer interiors (HV = 290) is slightly higher than that between layers (HV = 275). The energy-dispersive spectroscopy (EDS) measurements were performed on the α phase and β phase of the original specimen. The chemical composition of α phase (in wt pct) is: 90.88 Ti, 6.34 Al, 2.78 V and no trace of Fe. In the case of β phase, the composition (in wt pct) is: 82.57 Ti, 4.50 Al, 12.94 V and 0.15 Fe. Al is an α stabilizer, and V is a β stabilizer.
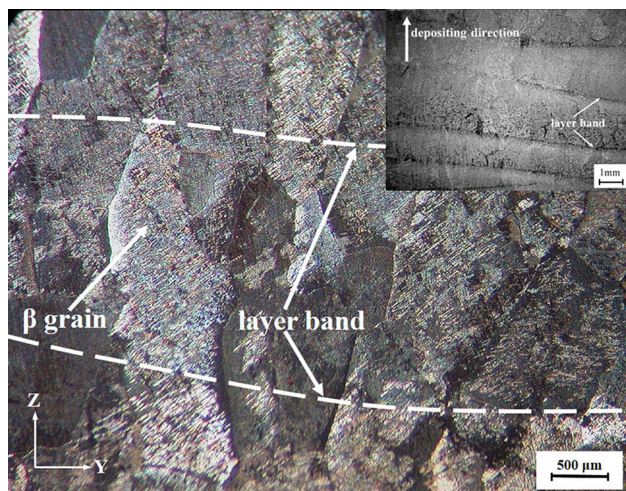
2.2 Compression Tests

We first conducted compression tests on the material. The static compression test was carried out with the strain rate of 0.001 s^{-1} by a DNS100 servohydraulic testing machine. The initial temperatures for the static compression test were selected to be 293, 573, 873 and 1173 K, respectively. The deformation of specimens was determined by subtracting the displacement due to the compliance of the loading frame from the
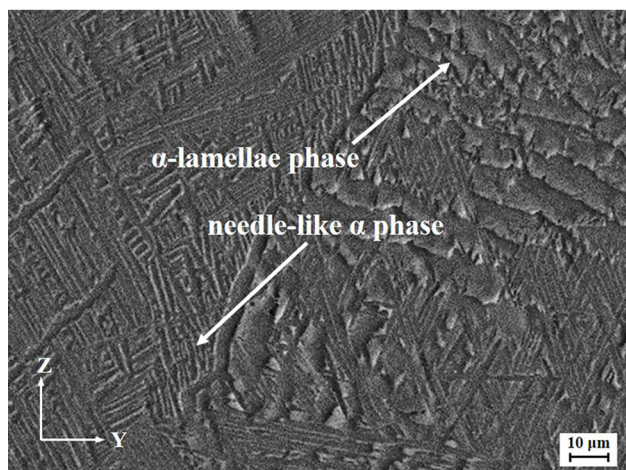
Table 1 Processing parameters of the LSF route

Laser power, kW	Scanning velocity, mm s^{-1}	Powder feed rate, g min^{-1}	Carrier gas flow, L h^{-1}	Laser spot diameter, mm	Increment of Z axis, mm
7	10-15	15-30	9-12	6	0.8-1.5

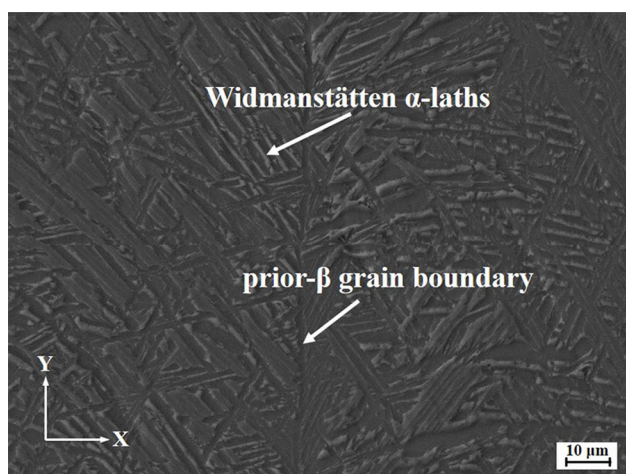displacement measured by the linear variable differential transducer (LVDT) mounted on the testing machine.

The dynamic compression test was carried out with the respective strain rates of 1000 and 5000 s^{-1} by NPU's enhanced split Hopkinson pressure bar system (Ref 10, 11), which was firstly developed by Nemat-Nasser and Isaacs (Ref 12, 13). The initial temperatures for the dynamic compression test were selected to be 173, 293, 573, 873 and 1173 K, respectively. The required high temperatures for the specimens were attained by using a radiant-heating furnace. The cylindrical specimens of Ti-6Al-4V alloy (LSF) for static and dynamic compression tests were prepared with the nominal dimensions of 5 mm in diameter and 4 mm in length, i.e., $\Phi 5$ mm $\times$ 4 mm.

2.3 Shear Tests

The static shear test was performed at the temperature of 293 K using the DNS100 servohydraulic testing machine. The dynamic shear test was performed by the enhanced split Hopkinson pressure bar system at strain rates of 10^5 s^{-1} order. For the purpose of discussing the influence of temperature and in consideration of the service temperature range of Ti-6Al-4V alloy, the initial temperatures for dynamic test were selected as 173, 293 and 573 K.

Hat-shaped specimens, originally developed by Meyer et al. (Ref 14), were used in both of the static and dynamic shear tests. The geometry of a hat-shaped specimen is axisymmetric and it consists of an upper "hat" portion and a lower "brim" portion with the shear region located at the transition part between the hat and the brim. The shape and dimensions of the specimen design are illustrated in Fig. 3.

All the hat-shaped specimens and cylindrical specimens were tested along the Y-direction and Z-direction. After that, the hat-shaped specimens were cut in half along the loading axis by electrical discharge machining. Then the specimens were ground lightly and polished. A solution of 46 mL H$_2$O + 3 mL HNO$_3$ + 1 mL HF was used to etch the specimens for three minutes until the microstructure was revealed. The metallographic analyses of the etched half sections were made by OM (NIKON SMZ800) and SEM (ZEISS SUPRA 55). The microhardness measurements were also obtained on

(a)

(b)

(c)

Fig. 2 Initial microstructure of Ti-6Al-4V alloy (LSF) in (a, b) *Y-Z* plane and (c) *X-Y* plane
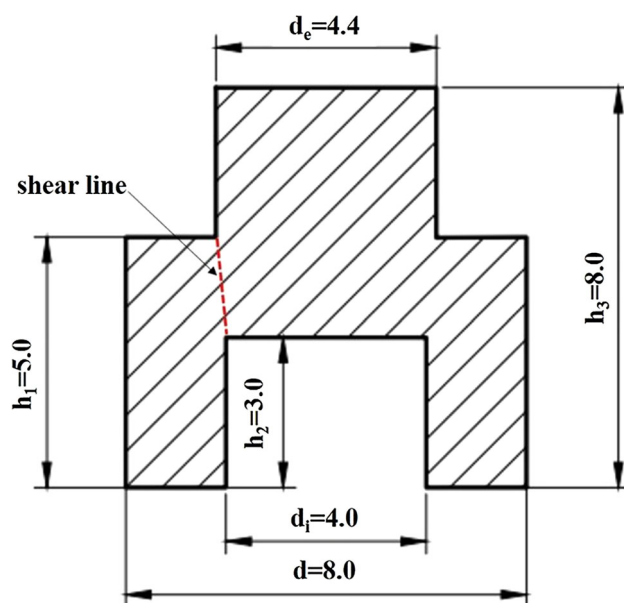
Fig. 3 Shape and dimensions of the hat-shaped specimen design (unit: mm)

the etched half sections with a Vickers diamond indenter at a load of 10 g for 10 s dwelling time.

3. Results and Discussion

3.1 Mechanical Response

Figure 4 shows the true stress-strain curves of cylindrical specimens under compression. The material constants of the Zerilli-Armstrong constitutive model were calibrated using these experimental data. In turn, this model was used to calculate the temperature rise in adiabatic shear bands of specimens during the shear deformation. These true stress-strain curves exhibit remarkable temperature sensitivity and strain rate sensitivity. For the compression test with strain rate of 5000 s^{-1}, the flow stress curves drop down slightly when the strain increases from 0.01 to 0.05. This phenomenon is caused by the dynamic recrystallization (DRX), which is the major deformation mechanism in the high-strain-rate loading process (Ref 6). The energy absorbed by each specimen until the adiabatic shearing failure is indicated by the area enclosed by the flow stress and the plastic strain. These areas are nearly the same along the Y-direction and Z-direction, which indicates that the propensity of adiabatic shear deformation and failure is also nearly the same along the two directions.

For the dynamic shear test on hat-shaped specimens, the shear displacement (Δu), the shear stress (τ), the nominal shear strain (γ) and the nominal shear strain rate ($\dot{\gamma}$) can be calculated as:
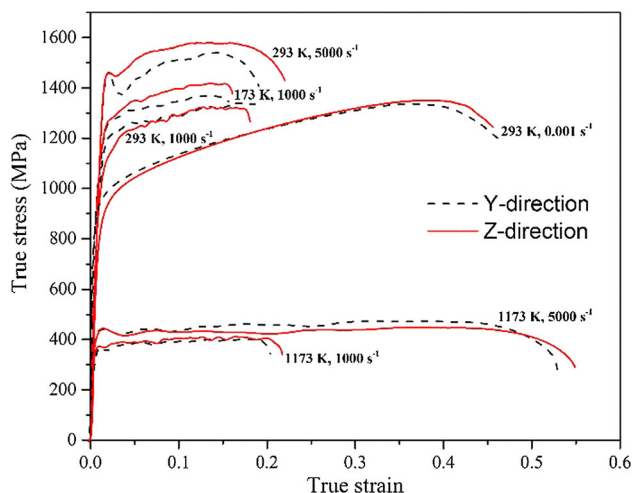
$$\Delta u = \int_0^t 2C_b\varepsilon_r \mathrm{d}t \qquad (\text{Eq 1})$$

$$\tau = E_b\left(\frac{A_b}{A_{SR}}\right)\varepsilon_t \qquad (\text{Eq 2})$$

$$\gamma = \Delta u/w \qquad (\text{Eq 3})$$

$$\dot{\gamma} = 2C_b\varepsilon_r/w \qquad (\text{Eq 4})$$

where C_b and E_b are the longitudinal elastic wave velocity and Young's modulus of Hopkinson bars, ε_r and ε_t are the re-flected and transmitted strain pulse in Hopkinson bars, A_b and A_{SR} are the area of Hopkinson bars and shear region, w is the width of adiabatic shear band (w is measured using OM and then confirmed by using SEM in the central area of each specimen).

The shear strain rates are estimated to be between 4.40×10^5 s^{-1} and 6.64×10^5 s^{-1}, which are extremely high compared with 0.001 s^{-1} during the static compression test. Table 2 shows the results together with the values of shear strain (γ) and longitudinal strain (ε). Based on the geometry, the shear strain (γ) can be related to the longitudinal strain (ε) as (Ref 15):

$$\varepsilon = \ln \sqrt{\gamma^2/2 + \gamma + 1} \qquad (\text{Eq 5})$$

The shear stress-displacement curves of hat-shaped specimens are shown in Fig. 5. It is noteworthy that the shear stress along the Y-direction and Z-direction are nearly the same despite the initial temperatures. The ultimate shear strength (the maximum in the shear stress-displacement curve) along the Z-direction is about 600 MPa at 573 K, whereas the ultimate shear strength is about 800 MPa at 173 K, corresponding to a 25% increase. Such observation indicates a significant increase in the shear stress with lower initial temperature. The Ti-6Al-4V alloy (LSF) still exhibits remarkable temperature sensitivity under high-strain-rate shear loading.

The shear stress can be converted into normal stress, σ, by the following formula:

$$\sigma = 2\tau. \qquad (\text{Eq 6})$$

The ultimate shear strength along the Y-direction is about 640 MPa at the temperature of 293 K, corresponding to a true stress of 1280 MPa. The stress level is in the same range of the strength measured for the cylindrical compression specimens at 293 K, which can be confirmed by the results shown in Fig. 4.

For the purpose of comparing the mechanical property, the shear stress-displacement curves of the conventional forged and extruded Ti-6Al-4V alloys were also analyzed. The hat-shaped specimen of the forged Ti-6Al-4V alloy, whose shape and dimensions are illustrated in Fig. 3, was tested under the condition of dynamic shear loading and initial temperature of 293 K. The corresponding data of the extruded Ti-6Al-4V alloy were obtained from the literature (Ref 7). As shown in Fig. 6, the ultimate shear strength is about 800 MPa for the forged Ti-6Al-4V alloy and 830 MPa for the extruded one. The curves of the LSFed and forged Ti-6Al-4V alloys share similar trend in shear stress but with different values. The ultimate shear strength is only about 640 MPa for Ti-6Al-4V alloy (LSF). These comparisons indicate that the ultimate shear strength of the Ti-6Al-4V alloy (LSF) is lower than that of the conventional forged and extruded Ti-6Al-4V alloys under dynamic shear loading.

A large variety of micro- and macroscale defects can arise in additively manufactured materials. The mechanical properties may thus be influenced by these defects. Zhao et al. (Ref 16) reported that the fatigue strength of the Ti-6Al-4V specimens prepared by selective laser melting and electron beam melting is lower than that of the cast and annealed alloys because of the pores contained in the as-fabricated specimens. Chen et al. (Ref 9) found that the stomatal defects within the microstructure of Ti60 alloy (LSF) lead to a sharp decrease in mechanical properties, and the defects have much greater influence than other microstructural features.

Fig. 4 Stress-strain response under comparison along Y-direction and Z-direction at selected initial temperatures and strain rates

Table 2 Experimental condition and deformation parameters for dynamic shear test

Specimen	Loading direction	Initial temp., K	w, μm	γ	ε	$\dot{\gamma}$, 10^5 s^{-1}
Y-1	Y-direction	173	30.1	11.0	2.14	6.64
Y-2	Y-direction	293	33.8	10.4	2.09	4.73
Y-3	Y-direction	573	28.6	33.2	3.19	5.24
Z-1	Z-direction	173	32.6	10.1	2.07	6.13
Z-2	Z-direction	293	36.4	9.62	2.02	4.40
Z-3	Z-direction	573	25.6	38.7	3.33	6.25
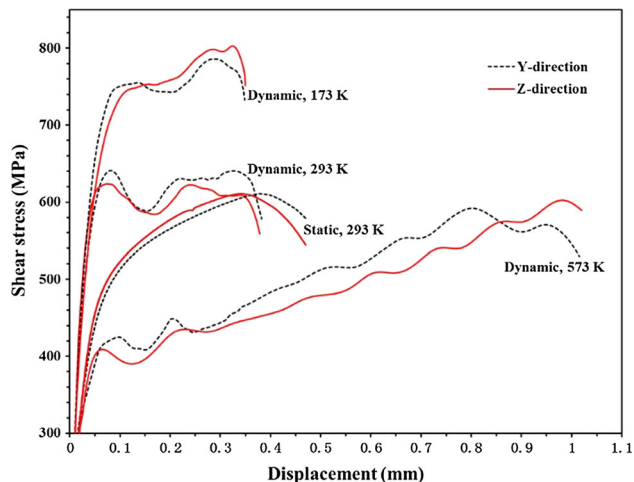
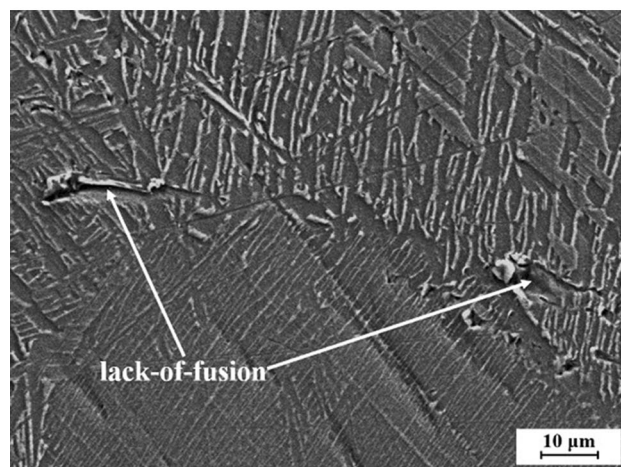Fig. 5 Shear stress vs. displacement curves of Ti-6Al-4V alloy (LSF)
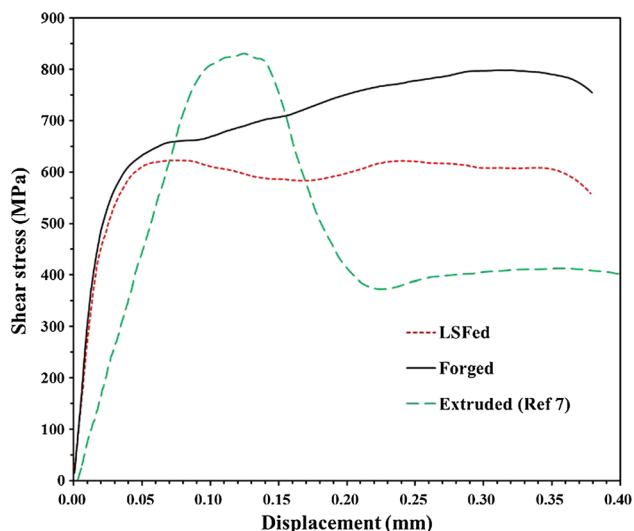
Fig. 6 Comparison of the shear response among the Ti-6Al-4V alloys fabricated by three different processes

(a)

(b)

Fig. 7 Initial defects of Ti-6Al-4V alloy (LSF). (a) Initial void; (b) Lack-of-fusion

The initial defects are still inevitable even though the technology of LSF has been improved greatly. Figure 7 shows the two main types of initial defects, namely initial void and lack-of-fusion (LoF). The shape of initial voids is cycloidal or elliptic and the diameter is about 1-10 μm. Such voids are so small that they cannot be detected by nondestructive testing techniques, such as x-ray or ultrasonic scan. The inwall of initial voids is quite smooth. The distribution of these voids in Ti-6Al-4V alloy (LSF) is fairly random. The initial voids may be caused by the gas that is entrapped in the hollow powders and remains after solidification due to the high cooling rate, or by the impurities in the powders (Ref 5, 17).

The presence of LoF may be attributed to the incomplete melting or the excessively high powder feeding rate. This type of defect is often in wedge shape or band shape and the inwall is relatively coarse, as shown in Fig. 7(b). This defect is known to be detrimental to mechanical properties. The sharp angles of the LoF defects may lead to local stress concentration during the loading process. These defects, therefore, may play an important role in early fracture, especially along the transverse direction (Ref 18). In general, the LoF defects are distributed on

the interface between the depositing layer and the substrate or between the two lower depositing layers, while they disappear in the higher depositing layers. It is difficult to prevent or even detect this type of defect without a destructive inspection.

These two types of defects are highly probable to serve as the nucleation sites for adiabatic shear bands and the sources for cracks in Ti-6Al-4V alloy (LSF) under high-strain-rate shear loading. Therefore, the observed difference in the dynamic shear strength between the Ti-6Al-4V alloy (LSF) and those fabricated by conventional processes is presumably caused by the initial defects in Ti-6Al-4V alloy (LSF).

In order to improve the shear resistance of Ti-6Al-4V alloy (LSF), the process control and process parameters are important to reduce the number of initial defects, such as initial void and LoF. The solutions to attenuate initial void mainly include: prolonging the existing time of melting pool, using the higher laser power and raising the loose density of Ti-6Al-4V alloy powders. To counteract the problem of LoF, the process parameters such as laser power, overlapping ratio and increment of Z axis should be optimized. The complete suppression of these defects may be achieved by carrying out hot isostatic pressing.

3.2 Microstructural Characteristics

Since the specimens underwent complex thermomechanical evolution during the dynamic shear deformation, the microstructure changed greatly in a very short time. Investigation of the residual microstructure by using OM and SEM is very helpful in understanding the evolution history and the effect of loading direction and initial temperature. After comparing the micrographs between specimens along the two different loading directions, it is found that the microstructural characteristics are similar regardless of the loading directions.

For comparison purpose, the microstructure of the statically loaded specimens was also examined. Figure 8 shows a typical micrograph of a specimen that was statically loaded in shear at the temperature of 293 K. It is evident that this specimen failed due to shear fracturing. This kind of fracturing is initiated by the intense flow instability due to the shear localization, and the shear localization initiates from the corners of specimens. As shown in Fig. 8, the shear deformation does not form an adiabatic shear band, but only distorts the initial microstructure of the specimen. There exist some discontinuous voids in front of the shear crack tip. In general, the voids are nucleated in circular or elliptical shape at the weak points within the shear region under static loading. Then these voids join together to be separate ligaments. A main crack along the shear line is thus formed (the shear line goes through the brim of hat-shaped specimen, as indicated in Fig. 3). Besides, there are a few initial voids distributed near the crack and in the shear region randomly.

Figure 9 shows the optical micrographs of adiabatic shear bands in the specimens, which were dynamically loaded at the temperatures being 173, 293 and 573 K, respectively. The adiabatic shear bands are long, narrow and straight bands that are distinguishable from the surrounding matrix. The width of the ASBs varies along their length. In addition, there are cracks forming in the far ends of the ASBs. The ASBs exhibit a few different external features for the specimens tested at different temperatures. As shown in Fig. 9(a) and (b), two ASBs exist within the specimens tested at 173 and 293 K, respectively.

They initiate at the corners of the specimens, where geometric imperfection may cause the strain concentration. The two ASBs expand very rapidly into the interior of the specimens along the maximum shear stress direction. Then they merge into one fully developed shear band that stretches from one corner to the other. Figure 9(c) shows the ASBs that initiate from both corners under the initial temperature of 573 K. In contrast to the well-defined coherent ASBs in Fig. 9(a) and (b), the ASBs shown in Fig. 9(c) are linked by a crack. They do not intersect into each other but propagate in their own paths. In the shear region, the cracks are formed not only at the corners (Fig. 9a and b) but at other location inside the shear band (Fig. 9c). The initiation of crack inside shear band may possibly be due to the aforementioned initial voids. The heat cannot release instantly because the high-strain-rate deformation is finished during a very short time. Therefore, the initial voids will serve as favorable sites for releasing the energy caused by the severe deformation, and the micro-cracks start to expand from these voids after accumulation of stress concentration.

The microstructure of specimen Z-1 (as listed in Table 2), which was deformed at 173 K, is shown in Fig. 10. It is observed that the location of shear band tip is not at the grain boundary. In front of the shear band tip there is an oval-shaped region, which is about 16.5 μm in length and about 8 μm in width. The EDS measurement was taken in this region, and the composition was found as (in wt pct): 88.62 Ti, 6.51 Al, 4.38 V and 0.33 Fe. The shape and dimension as well as the composition of this region indicate that it can possibly be an initial defect, namely the lack-of-fusion. Generally, the grains in shear band are seriously elongated and refined under the dynamic shear loading. This lack-of-fusion defect still remains intact, but some microcracks seem to appear on its surface. This defect, directly located in front of the shear crack, neither promotes any new crack initiation nor makes the shear band deflected. Therefore, such defect configuration here does not dramatically lower the local toughness of the material.

Similar characteristics is observed in specimen Y-2, which was deformed under the loading condition of 4.73×10^5 s^{-1} and 293 K, as shown in Fig. 11. No distinct difference in the microstructural characteristics is found between specimens tested under room temperature and 173 K. It indicates that the influence of initial temperature on the microstructural evolution is not significant. It is well known that the shear localization may come into being before the failure initiations, such as voids and cracks. As shown in Fig. 11, a well-developed shear band is accompanied by voids and cracks within it. The formation of these voids is probably related to the stress concentration caused by severe shear-deformation inhomogeneity in the microscopic defects. The voids may also be form as a direct consequence of thermal softening due to the high temperature in ASBs (Ref 19). All these voids possess smooth surfaces and they may nucleate, grow and eventually coalesce to form cracks.

The adiabatic shear band in Y-2 specimen was magnified under SEM (Fig. 12). It is shown that the microstructure pattern of the central ASB is different from that of the boundary. The central ASB structure is refined, and it is too dense to be distinguished even with SEM. Some voids are found in the interface between the ASB and the matrix material. The nucleation of voids is considered as the result of the tensile stress in ASBs (Ref 20). Due to the relatively lower temperature of the boundary, the strength of the boundary is higher than that
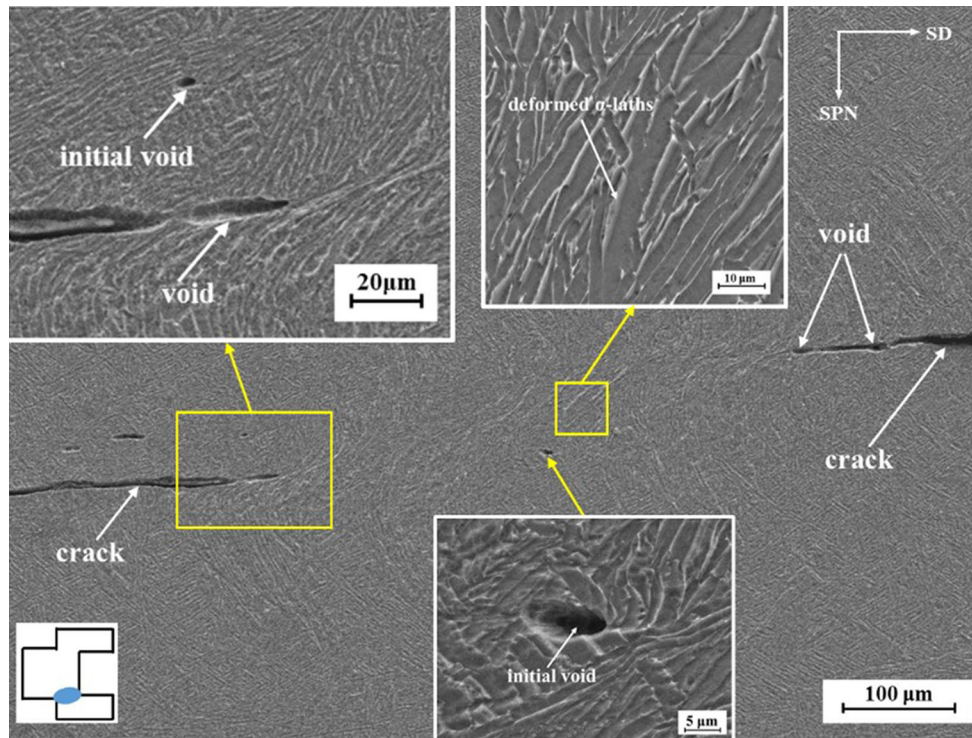
Fig. 8 Microstructure of the failed specimen under static shear at the temperature of 293 K. The hat schematic indicates the region photographed. The shear direction (SD) is the horizontal one. SPN strands for the shear normal plane

of the material in the ASB during the high-speed plastic deformation (Ref 20, 21). Thus, the material in the interface is relatively weak and it favors the nucleation of voids. One initial void is also found near the shear band. This type of voids will have influence on the material strength if they are just located inside or very close to the shear band.

Figure 13 illustrates the microhardness distribution inside and near the adiabatic shear band of specimen *Y*-2. The microhardness inside the ASB is up to 330 HV in contrast to the surrounding matrix (approximately 280 HV). The hardness change observed in this work agrees well with the results of earlier studies (Ref 22, 23), which indicates that the hardness inside the adiabatic shear band is higher than that of the surrounding matrix. This observation of increased microhardness suggests that the grains inside the shear band have been refined by the strong shear deformation, resulting in the reduction in grain size (Ref 24).

To better understand the dynamic deformation characteristics at higher temperature, we carried out the microstructural analysis of specimen *Y*-3 under the loading condition of 593 K and 5.24×10^5 s^{-1}. The result is shown in Fig. 14. Two cracks are clearly observed near the ASB. One crack is located in front of ASB, and the other deviates from the direction of ASB. The shear band is a preferred path for crack propagation at large imposed shear strains (Ref 25, 26). The crack which deviates from the direction of ASB presumably results from the initial defects near the shear region, and it propagates in the region where the stress level is very low. Finally, the crack stops propagating inside the specimen. As a consequence, the shear resistance of Ti-6Al-4V alloy (LSF) can be effectively improved by adjusting the processing parameters of the LSF technology to reduce the number of initial defects.

### 3.3 Dynamic Recrystallization in the Adiabatic Shear Band

The temperature rise in the adiabatic shear band is an important parameter in the investigation of the microstructural evolution. While the strain rate is higher than 10^3 s^{-1}, the deformation process of shear region will become very fast and can be essentially considered as an adiabatic process. As the temperature rise in specimens is difficult to be measured directly due to the short duration of the test, the value of temperature (T) in adiabatic shear band is expressed by an integral equation:

$$T = T_0 + \left(\frac{\beta}{\rho C_P}\right) \int_0^\varepsilon \sigma \mathrm{d}\varepsilon, \qquad \text{(Eq 7)}$$

where T_0 is the initial temperature, ρ the density (4.43 g cm^{-3}), C_P the heat capacity, β the fraction of plastic energy converted into heat, σ the stress and ε the strain. Though determination of the heat conversion factor is still an ongoing discussion, the value of β is often presumed to be between 0.9 and 1 (Ref 27). In this work, $\beta = 0.9$ was chosen. For Ti-6Al-4V alloys, the temperature dependence of C_P must be considered as its value may change from 0.58 J g^{-1} K^{-1} (20 °C) to 0.93 J g^{-1} K^{-1} (870 °C) (Ref 28). Thus, the heat capacity $C_P(T)$ is given as (Ref 20):

$$C_P(T) = 0.559 + 1.357 \times 10^{-4} T - 3.366 \times 10^3 / T^2 \\ + 2.767 \times 10^{-8} T^2 [\text{J/g K}] \qquad \text{(Eq 8)}$$

Because of the uncertainties related to the shear area and the shear displacement in hat-shaped specimens, the temperature rise was estimated by integrating the Zerilli-Armstrong constitutive equation with the deformation conditions. This constitutive equation is as follows (Ref 29):
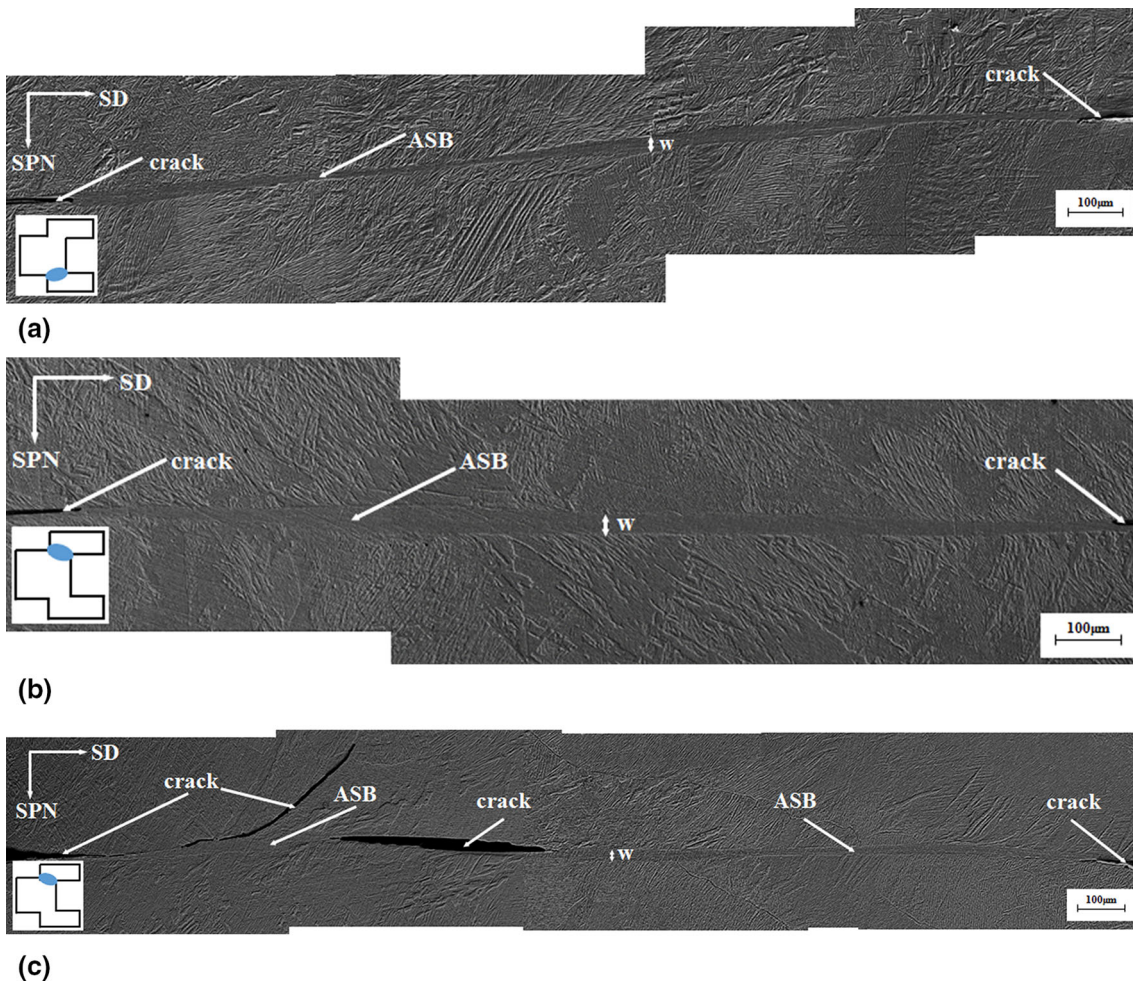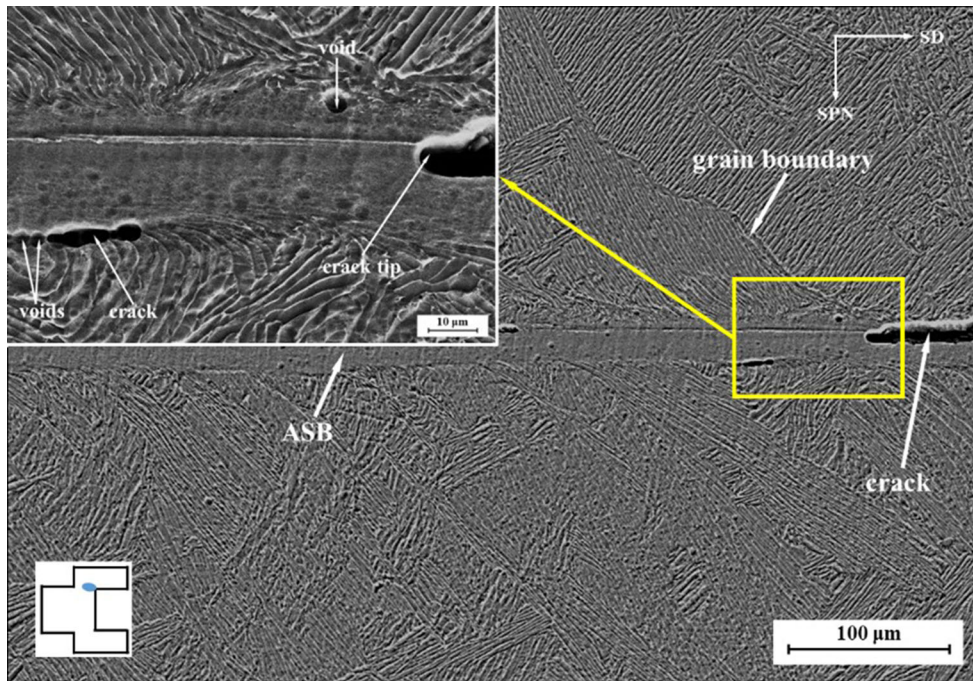
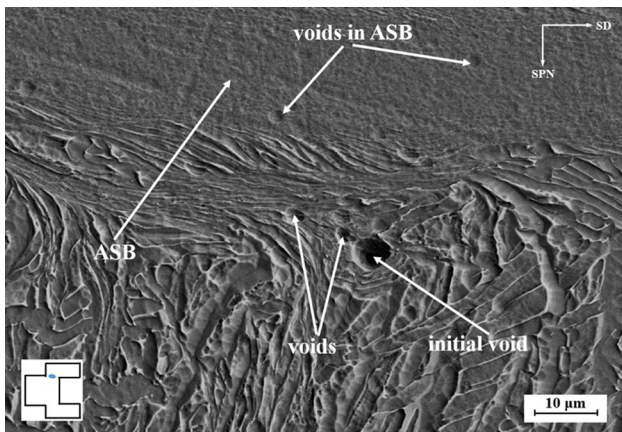**Fig. 9** Micrographs of adiabatic shear bands in specimens tested under: (a) 173 K; (b) 293 K; (c) 573 K
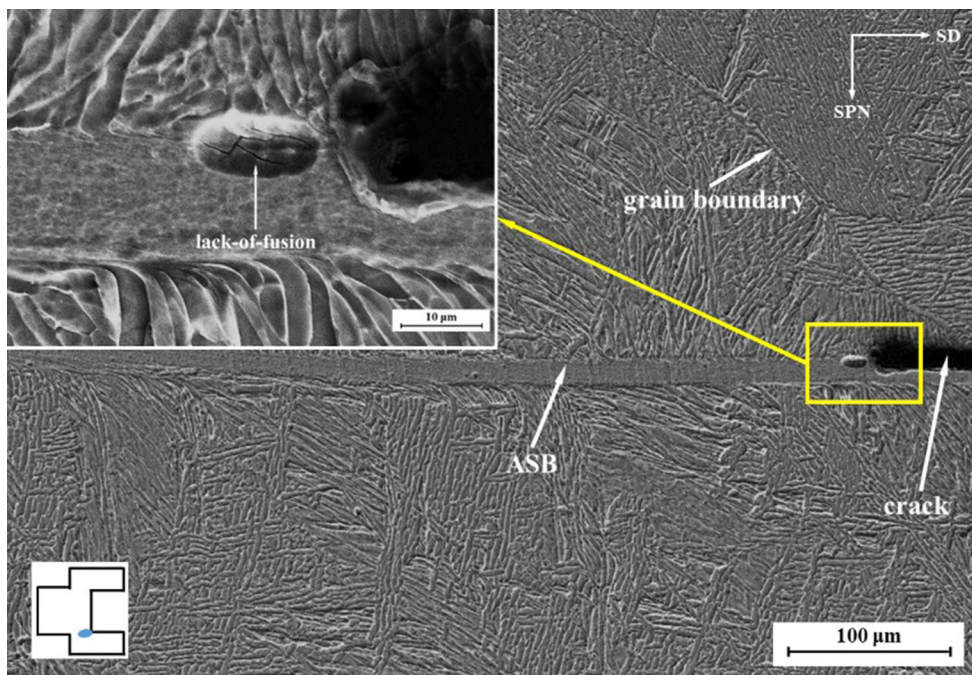
Fig. 10 SEM micrograph of the specimen tested under the temperature of 173 K and strain rate of 6.13×10^5 s^{-1}

Fig. 11 SEM micrograph of the specimen tested under the temperature of 293 K and strain rate of 4.73×10^5 s^{-1}
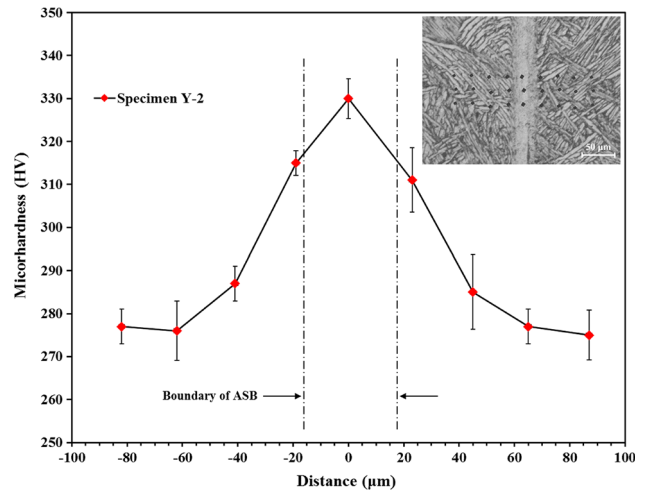

Fig. 12 SEM micrograph of the adiabatic shear band within the specimen tested under the temperature of 293 K and strain rate of 4.73×10^5 s^{-1}

Fig. 13 Microhardness as a function of distance across the middle of shear band

$$\sigma = C_0 + B_0 \varepsilon^{C_n} \exp[-\alpha_0 T + \alpha_1 T \ln(\dot{\varepsilon})] + B \exp[-\beta_0 T + \beta_1 T \ln(\dot{\varepsilon})],$$
(Eq 9)

where C_0, C_n, B_0, B, α_0, α_1, β_0 and β_1 are the material constants obtained by regression analysis based on the stress-strain data provided mainly in Fig. 4. The final strain (ε) in Eq 7 can be calculated by converting the shear strain in adiabatic shear band into the longitudinal strain based on Eq 5. The calculated strain (ε) is listed in Table 2. The stress (σ) is determined by using the Zerilli-Armstrong constitutive equation (Eq 9).

It is noteworthy that the maximum temperature in the adiabatic shear band of specimen Y-2 is about 1120 K. The temperature that marks the onset of thermal recovery/recrystallization process in metallic materials is usually given by

$T_{Re} = (0.4 - 0.5)T_m$, where T_m is the melting temperature. For Ti-6Al-4V alloy, the value of T_{Re} usually ranges from 770 to 963 K. Therefore, the temperature in shear band can exceed the recrystallization temperature. By examining the microstructure, the microhardness and the temperature in the adiabatic shear band, we found that dynamic recrystallization (DRX) is most likely the main process of the microstructural evolution.

As a matter of fact, many researchers agree that, in a large number of metallic materials, dynamic recrystallization takes place inside the shear bands during deformation (Ref 30-32). Peirs et al. (Ref 33) studied the shear bands in Ti-6Al-4V alloy by using the hat-shaped specimens under high-strain-rate compression with a split Hopkinson pressure bar setup. The results show that recrystallization occurs after strain localization in the core region of adiabatic shear band. Rittel et al. (Ref
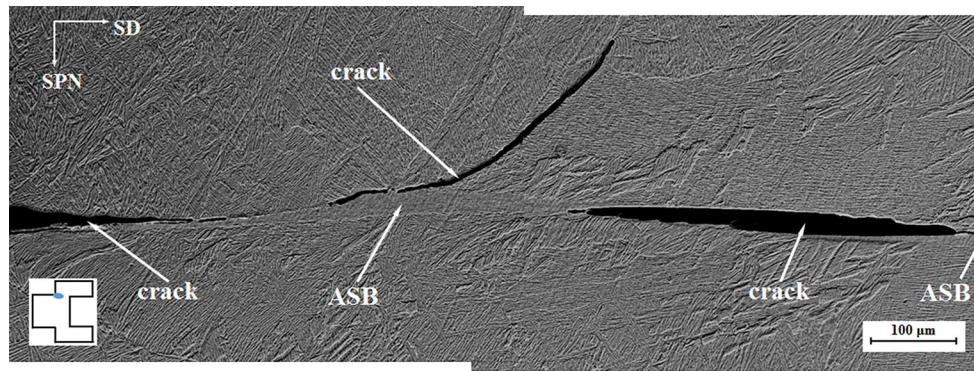
Fig. 14 SEM micrograph of the specimen tested under the temperature of 573 K and strain rate of $5.24 \times 10^5 \text{ s}^{-1}$

[34]) observed the nanograins in shear compression samples of Ti-6Al-4V alloy. They concluded that DRX not only precedes the adiabatic shear failure, but it is also likely to serve as a dominant micromechanical factor in the very generation of the band. Landau et al. (Ref [35]) investigated the microstructural evolution of Ti-6Al-4V specimens subjected to high-strain-rate deformation and reported that the DRX grains are formed in the early stages of deformation.

To distinguish whether the static recrystallization is involved during the formation process of fine grains in shear band, the Fourier heat conduction equations are used to calculate the temperature during the cooling stage. The equations are (Ref [36]):

$$\rho C_\text{P} \frac{\partial T}{\partial t} = K_0 \nabla^2 T + \tau \dot{\gamma} \qquad \text{(Eq 10a)}$$

and

$$\nabla^2 \equiv \frac{1}{r_\text{p}} \frac{\partial}{\partial r_\text{p}} \left(r_\text{p} \frac{\partial}{\partial r_\text{p}} \right) + \frac{1}{r_\text{p}^2} \frac{\partial^2}{\partial \theta_\text{p}^2}, \qquad \text{(Eq 10b)}$$

where the thermal conductivity, K_0, is 3.07 W/(m K) and $(r_\text{p}, \theta_\text{p})$ are the polar coordinates.

An acceptable estimation can be obtained by using a one-dimensional calculation that considers a small shear band in an infinite medium, because the shear band is quite narrow and axially symmetric. Presuming a constant rate of the heat generation and a uniform distribution of temperature in the narrow shear band, the solution of the heat equation can be simplified as the following expression (Ref [36]):

$$T(x,t) = \frac{2d_\text{s}(t_\text{max} - T_0)}{\sqrt{4\pi kt}} e^{-(x - R_\text{i})^2/4kt} (R_\text{i} - d_\text{s} < x < R_\text{i} + d_\text{s}) \qquad \text{(Eq 11)}$$

where the material constant, k, is equal to $K_0/(\rho \cdot C_\text{P})$, T_max is the maximum temperature in shear band, d_s the half-width of shear band and R_i the distance from the center of shear band to the center of specimen. These parameters used in Eq 11 are set as $T_\text{max} = 1120 \text{ K}$, $T_0 = 293 \text{ K}$, $d_\text{s} = 16.9 \text{ μm}$ and $R_\text{i} = 2.1 \text{ mm}$. The value of x is set as 1.2 mm to study the cooling stage in the core region of shear band. It takes about 590 μs for the adiabatic shear band to cool down from 1120 K to the initial temperature of 293 K after the shear localization process ceases. The cooling rate is about

1.4×10^6 K/s, which is very high. Thus, the effect of static recrystallization on the microstructure can be neglected during such a short time.

Several previous investigations reported the onset of recrystallization under the high-strain-rate conditions in many metallic materials (Ref [30], [31], [37]). The theory named as rotational dynamic recrystallization (RDR), proposed originally by Derby (Ref [38]) and modified afterward by Meyers et al. (Ref [39]), is able to describe the nature of such kinetic process quite well. According to the RDR theory, the formation of new grains needs the rotation of local grain boundaries driven by the minimization of interfacial energy. The time (t) required for this process can be determined by the following equation (Ref [31]):

$$t = \frac{L_1 k T f(\theta)}{4\delta \eta D_\text{b0} \exp(-Q_\text{b}/RT)}, \qquad \text{(Eq 12)}$$

where δ is the grain boundary thickness, η the grain boundary energy, D_b0 a constant associated with grain boundary diffusion, Q_b the activation energy for grain boundary diffusion, L_1 the average diameter of subgrains and θ the subgrain misorientation. Here the value of Q_b is equal to (0.4-0.6) Q, and Q is the activation energy for grain growth. The function $f(\theta)$ is given by

$$f(\theta) = \frac{3\tan(\theta) - 2\cos(\theta)}{3 - 6\sin(\theta)} + \frac{2}{3} - \frac{4\sqrt{3}}{9} \ln \frac{2 + \sqrt{3}}{2 - \sqrt{3}}$$
$$+ \frac{4\sqrt{3}}{9} \ln \frac{\tan(\theta/2) - 2 - \sqrt{3}}{\tan(\theta/2) - 2 + \sqrt{3}}. \qquad \text{(Eq 13)}$$

Since there are no kinetic parameters available for Ti-6Al-4V alloy (LSF) currently, the parameters of the commercial pure titanium are used instead: $\delta = 6.0 \times 10^{-10}$ m, $\eta = 1.19$ J/m^2, $D_\text{b0} = 1.0 \times 10^{-5}$ m^2/s, $Q = 204$ kJ/mol, k = 1.38×10^{-23} J/K and R = 8.314 J/(mol K) (Ref [40]). The subgrain boundaries need to rotate approximately 30° to form recrystallized grains according to the RDR theory. Thus, the kinetic curves for the RDR process can be obtained by substituting these parameters into Eq 12 and the results are shown in Fig. 15(a) and (b). In Fig. 15(a), the temperature varies from 0.40 T_m to 0.50 T_m for the subgrain of 0.1 μm in size; in Fig. 15(b), the subgrain size, L_1, varies from 0.1 μm to 1.0 μm at $T/T_\text{m} = 0.50$ (963 K). These results indicate that the fine grains ranging from 0.1 to 1.0 μm can be formed within 10 μs by the grain boundaries rotation. Moreover, under higher temperatures, less time is needed to form the grains of the same
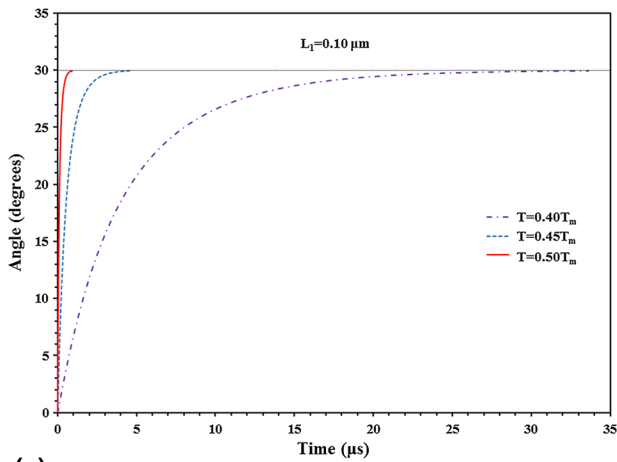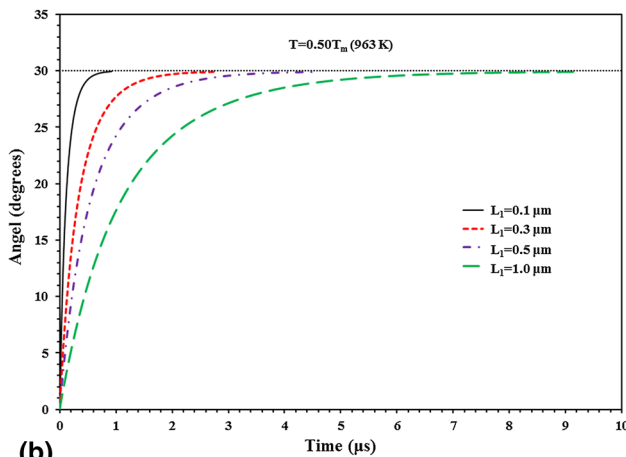
Fig. 15 Angle of rotation of the subgrain boundaries in Ti-6Al-4V alloy (LSF) as a function of the required time for (a) different temperatures $(L_1 = 0.10 \ \mu m)$ and (b) different subgrain sizes $(T = 0.50 \ T_m)$

size. The time for plastic deformation (t_{PD}) to occur can be determined by dividing the displacement (given by Eq 1) by the velocity of the incident bar (v): $t_{PD} = \Delta u / v$. For specimen Y-2, the deformation time is about 22 μs. It is longer than the time needed for the RDR process. Therefore, the RDR process is kinetically possible and the fine grains in adiabatic shear band can be formed by grain boundaries rotation during the deformation process. Moreover, the fine recrystallized grains may rotate during the rest time of deformation and coalesce along the shear direction (Ref 41-43). However, the newly recrystallized grains rarely undergo remarkable growth by grain boundary migration during the cooling stage due to the high-speed cooling and the lack of drive force (Ref 44, 45).

4. Conclusions

In this study, the hat-shaped specimens of Ti-6Al-4V alloy (LSF) were dynamically and statically sheared at various initial temperatures with a servohydraulic testing machine and an enhanced split Hopkinson pressure bar system. The microstructural characteristics of both the original and deformed specimens were investigated. The dynamic recrystallization process in the adiabatic shear band was discussed.

The following conclusions can be made based on this work:

1. No distinct anisotropy of the shear properties is found in Ti-6Al-4V alloy (LSF) despite the visible stratification and the prior-β grains that grow epitaxially along the depositing direction.
2. There is remarkable temperature sensitivity of Ti-6Al-4V alloy (LSF) under dynamic shear loading. This alloy possesses lower dynamic shear strength than the conventional forged and extruded Ti-6Al-4V alloys. Such difference presumably results from the initial defects in Ti-6Al-4V alloy (LSF).
3. The adiabatic shear bands can be formed under the dynamic shear loading. They are straight, long and narrow bands of 25.6-36.4 μm approximately in width. The microstructure inside the shear bands cannot be identified even with SEM at high magnification. The microhardness test shows that the hardness inside the adiabatic shear band is higher than that of the surrounding matrix. Such phenomenon is caused by the strengthening effect of the grain refinement.
4. The temperature in adiabatic shear band is calculated to be about 1120 K, which is higher than the recrystallization temperature. The high cooling rate estimated by the Fourier heat conduction equations indicates that the effect of static recrystallization on the microstructure can be neglected. The formation kinetics of the fine grains can be described by the rotational dynamic recrystallization theory. These results together with the microstructural observations confirm that the grain refinement in the adiabatic shear band is caused by rotational dynamic recrystallization.

References

1. M.L. Griffith, L.D. Harwell, and J.A. Romero, Multi-Material Processing by LENS, Proceedings of the Solid Freeform Fabrication Symposium, *Univ. Tex.*, 1997, **1997**, p 387–393
2. M.L. Griffith, M.E. Schlienger, L.D. Harwell, M.S. Oliver, M.D. Baldwin, M.T. Ensz, M. Essien, J. Brooks, C.V. Robino, J.E. Smugeresky, W.H. Hofmeister, M.J. Wert, and D.V. Nelson, Understanding Thermal Behavior in the LENS Process, *Mater. Des.*, 1999, **20**(2), p 107–113
3. P.A. Kobryn, E.H. Moore, and S.L. Semiatin, The Effect of Laser Power and Traverse Speed on Microstructure, Porosity, and Build Height in Laser-Deposited Ti-6Al-4V, *Scr. Mater.*, 2000, **43**(4), p 299–305
4. S. Bontha, N.W. Klingbeil, P.A. Kobryn, and H.L. Fraser, Thermal Process Maps for Predicting Solidification Microstructure in Laser Fabrication of Thin-Wall Structures, *J. Mater. Process. Technol.*, 2006, **178**(1), p 135–142
5. S. Zhang, X. Lin, J. Chen, and W. Huang, Effect of Solution Temperature and Cooling Rate on Microstructure and Mechanical Properties of Laser Solid Forming Ti-6Al-4V Alloy, *Chin. Opt. Lett.*, 2009, **7**(6), p 498–501

6. P.H. Li, W.G. Guo, W.D. Huang, Y. Su, X. Lin, and K.B. Yuan, Thermomechanical Response of 3D Laser-Deposited Ti–6Al–4V Alloy Over a Wide Range of Strain Rates and Temperatures, *Mater. Sci. Eng. A*, 2015, **647**, p 34–42

7. J. Peirs, P. Verleysen, J. Degrieck, and F. Coghe, The Use of Hat-Shaped Specimens to Study the High Strain Rate Shear Behaviour of Ti–6Al–4V, *Int. J. Impact Eng.*, 2010, **37**(6), p 703–714

8. J. Peirs, P. Verleysen, J. Degrieck, and F. Coghe, Novel Technique for Static and Dynamic Shear Testing of Ti6Al4V Sheet, *Exp. Mech.*, 2012, **52**(7), p 729–741

9. J. Chen, R. Zhang, Q. Zhang, J. Yang, and W. Huang, Relationship Among Microstructure, Defects and Performance of Ti60 Titanium Alloy Fabricated by Laser Solid Forming, *Rare Met. Mater. Eng.*, 2014, **43**(3), p 548–552

10. J.J. Wang, W.G. Guo, J. Guo, Z.A. Wang, and S.L. Lu, The Effects of Stress Triaxiality, Temperature and Strain Rate on the Fracture Characteristics of a Nickel-Base Superalloy, *J. Mater. Eng. Perform.*, 2016, **25**, p 2043–2052

11. J.J. Wang, W.G. Guo, X.S. Gao, and J. Su, The Third-Type of Strain Aging and the Constitutive Modeling of a Q235B Steel Over a Wide Range of Temperatures and Strain Rates, *Int. J. Plast.*, 2015, **65**, p 85–107

12. S. Nemat-Nasser and J.B. Isaacs, Direct Measurement of Isothermal Flow Stress of Metals at Elevated Temperatures and High Strain Rates with Application to Ta and Ta-W Alloys, *Acta Mater.*, 1997, **45**(3), p 907–919

13. S. Nemat-Nasser and W.G. Guo, Thermomechanical Response of DH-36 Structural Steel Over a Wide Range of Strain Rates and Temperatures, *Mech. Mater.*, 2003, **35**(11), p 1023–1047

14. M.A. Meyers, K.P. Staudhammer, and L.E. Murr, Ed., *Metallurgical Applications of Shock-Wave and High-Strain-Rate Phenomena*, Marcel Dekker, New York, NY, 1986, p 657–674

15. R. Culver, *Thermal Instability Strain in Dynamic Plastic Deformation, Metallurgical Effects at High Strain Rates*, Springer US, Berlin, 1973, p 519–530

16. X. Zhao, S. Li, M. Zhang, Y. Liu, T.B. Sercombe, S. Wang, Y. Hao, R. Yang, and L.E. Murr, Comparison of the Microstructures and Mechanical Properties of Ti-6Al-4V Fabricated by Selective Laser Melting and Electron Beam Melting, *Mater. Des.*, 2016, **95**, p 21–31

17. X. Lin, T.M. Yue, H.O. Yang, and W.D. Huang, Solidification Behavior and the Evolution of Phase in Laser Rapid Forming of Graded Ti6Al4V-Rene88DT Alloy, *Metall. Mater. Trans. A*, 2007, **38**(1), p 127–137

18. T. Vilaro, C. Colin, and J.D. Bartout, As-Fabricated and Heat-Treated Microstructures of the Ti-6Al-4V Alloy Processed by Selective Laser Melting, *Metall. Mater. Trans. A*, 2011, **42**(10), p 3190–3199

19. X. Liu, C. Tan, J. Zhang, F. Wang, and H. Cai, Correlation of Adiabatic Shearing Behavior with Fracture in Ti-6Al-4V Alloys with Different Microstructures, *Int. J. Impact Eng.*, 2009, **36**(9), p 1143–1149

20. Q. Xue, M.A. Meyers, and V.F. Nesterenko, Self-Organization of Shear Bands in Titanium and Ti-6Al-4V Alloy, *Acta Mater.*, 2002, **50**(3), p 575–596

21. Y. Yang, X.M. Li, X.L. Tong, Q.M. Zhang, and C.Y. Xu, Effects of Microstructure on the Adiabatic Shearing Behaviors of Titanium Alloy, *Mater. Sci. Eng. A*, 2011, **528**(7), p 3130–3133

22. W.S. Lee, C.F. Lin, T.H. Chen, and H.H. Hwang, Correlation of Dynamic Impact Properties with Adiabatic Shear Banding Behaviour in Ti-15Mo-5Zr-3Al Alloy, *Mater. Sci. Eng. A*, 2008, **475**(1), p 172–184

23. D. Yang, Y. An, P. Cizek, and P. Hodgson, Development of Adiabatic Shear Band in Cold-Rolled Titanium, *Mater. Sci. Eng. A*, 2011, **528**(12), p 3990–3997

24. F. Yuan, P. Jiang, and X. Wu, Annealing Effect on the Evolution of Adiabatic Shear Band Under Dynamic Shear Loading in Ultra-Fine-Grained Iron, *Int. J. Impact Eng.*, 2012, **50**, p 1–8

25. M.A. Meyers, G. Subhash, B.K. Kad, and L. Prasad, Evolution of Microstructure and Shear-Band Formation in α-hcp Titanium, *Mech. Mater.*, 1994, **17**(2), p 175–193

26. H.A. Grebe, H.R. Pak, and M.A. Meyers, Adiabatic Shear Localization in Titanium and Ti-6 pct Al-4 pct V Alloy, *Metall. Trans. A*, 1985, **16**(5), p 761–775

27. R. Kapoor and S. Nemat-Nasser, Determination of Temperature Rise During High Strain Rate Deformation, *Mech. Mater.*, 1998, **27**(1), p 1–12

28. ASM Committee on Titanium and Titanium Alloys, *Metals Handbook*, Vol 3, 9th ed., ASM International, Metals Park, OH, 1980

29. F.J. Zerilli and R.W. Armstrong, Shock Compression of Condensed Matter, AIP Conference Proceedings (No. 370). Seattle, WA, 1995, AIP, 1996, p 31–35

30. J.A. Hines and K.S. Vecchio, Recrystallization Kinetics Within Adiabatic Shear Bands, *Acta Mater.*, 1997, **45**(2), p 635–649

31. M.A. Meyers, Y.B. Xu, Q. Xue, M.T. Perez-Prado, and T.R. McNelley, Microstructural Evolution in Adiabatic Shear Localization in Stainless Steel, *Acta Mater.*, 2003, **51**(5), p 1307–1325

32. S.N. Medyanik, W.K. Liu, and S. Li, On Criteria for Dynamic Adiabatic Shear Band Propagation, *J. Mech. Phys. Solids*, 2007, **55**(7), p 1439–1461

33. J. Peirs, W. Tirry, B. Amin-Ahmadi, F. Coghe, P. Verleysen, L. Rabet, and J. Degrieck, Microstructure of Adiabatic Shear Bands in Ti6Al4V, *Mater. Charact.*, 2013, **75**, p 79–92

34. D. Rittel, P. Landau, and A. Venkert, Dynamic Recrystallization as a Potential Cause for Adiabatic Shear Failure, *Phys. Rev. Lett.*, 2008, **101**(16), p 165501-1–p165501-4

35. P. Landau, A. Venkert, and D. Rittel, Microstructural Aspects of Adiabatic Shear Failure in Annealed Ti6Al4V, *Metall. Mater. Trans. A*, 2010, **41**(2), p 389–396

36. S. Nemat-Nasser, J.B. Isaacs, and M. Liu, Microstructure of High-Strain, High-Strain-Rate Deformed Tantalum, *Acta Mater.*, 1998, **46**(4), p 1307–1325

37. M.T. Perez-Prado, J.A. Hines, and K.S. Vecchio, Microstructural Evolution in Adiabatic Shear Bands in Ta and Ta-W Alloys, *Acta Mater.*, 2001, **49**(15), p 2905–2917

38. B. Derby, The Dependence of Grain Size on Stress During Dynamic Recrystallization, *Acta Metall. Mater.*, 1991, **39**(5), p 955–962

39. M.A. Meyers, V.F. Nesterenko, J.C. LaSalvia, Y.B. Xu, and Q. Xue, Observation and Modeling of Dynamic Recrystallization in High-Strain, High-Strain Rate Deformation of Metals, *J. Phys. IV Fr.*, 2000, **10**, p 9-51–9-56

40. Q.L. Yong, J.G. Tian, and W. Yang, Physical Metallurgical Data of Titanium in Steel, *J. Yunnan Polytech. Univ.*, 1999, **15**(2), p 7–10

41. B.F. Wang, Z.L. Liu, X.Y. Wang, and Z.Z. Li, An EBSD Investigation on Deformation-Induced Shear Bands in a Low Nickel Austenitic Stainless Steel Under Controlled Shock-Loading Conditions, *Mater. Sci. Eng. A*, 2014, **610**, p 301–308

42. D. Jia, Y.M. Wang, K.T. Ramesh, E. Ma, Y.T. Zhu, and R.Z. Valiev, Deformation Behavior and Plastic Instabilities of Ultrafine-Grained Titanium, *Appl. Phys. Lett.*, 2001, **79**(5), p 611–613

43. Y.M. Wang, E. Ma, and M.W. Chen, Enhanced Tensile Ductility and Toughness in Nanostructured Cu, *Appl. Phys. Lett.*, 2002, **80**(13), p 2395–2397

44. Y. Yang, F. Jiang, B.M. Zhou, X.M. Li, H.G. Zheng, and Q.M. Zhang, Microstructural Characterization and Evolution Mechanism of Adiabatic Shear Band in a Near beta-Ti Alloy, *Mater. Sci. Eng. A*, 2011, **528**(6), p 2787–2794

45. B. Wang, J. Li, J. Sun, X. Wang, and Z. Liu, Shear Localization and Its Related Microstructural Evolution in the Ultrafine Grained Titanium Processed by Multi-Axial Compression, *Mater. Sci. Eng. A*, 2014, **612**, p 227–235